Journal of Energy Storage 132 (2025) 117652



Contents lists available at ScienceDirect

Journal of Energy Storage

journal homepage: www.elsevier.com/locate/est

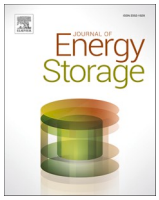

Research papers

Simulations-based investigation of thermal runaway onset and propagation in a Li-ion battery pack with phase transition interstitial material

Muhammad Mehdi Abbas [a], Dhananjay Mishra [a], Emad Hasrati [a], Byoungchul Kwon [b], Vinay Premnath [b], Judith Jeevarajan [b], Ankur Jain [a,*]

[a] Mechanical and Aerospace Engineering Department, University of Texas at Arlington, Arlington, TX, USA
[b] Electrochemical Safety Research Institute, UL Research Institutes, Houston, TX, USA

ARTICLE INFO

Keywords:
Li-ion cells
Battery pack
Thermal runaway
Simulation modeling
Phase transition materials

ABSTRACT

Thermal runaway propagation in Lithium-ion (Li-ion) battery packs is an important safety concern in electrochemical energy storage. In addition to insights from safety tests, accurate and efficient numerical simulations can also help fully understand this critical failure mechanism. This study presents a numerical simulation for predicting the temperature field and thermal runaway characteristics in a battery pack of cylindrical Li-ion cells that includes a phase transition material between cells. Simulation results are compared with experimental data from an abuse test involving twenty-five 18650 Li-ion cells connected in parallel and separated by a phase transition material within a shipping box. The impact of thermophysical properties — thermal conductivity, specific heat capacity, latent heat, and phase transition temperature of the interstitial material — on thermal runaway propagation is investigated. Results show that thermal conductivity of the interstitial material plays an important role in mitigating thermal runaway propagation. In contrast, the effect of other properties is much less critical. This simulation model offers versatile predictive capability across various scenarios involving thermal abuse of Li-ion battery packs. Moreover, the numerical simulation developed in this study may provide insights into the thermal behavior of the phase transition material, towards effective thermal management systems for Li-ion battery packs.

1. Introduction

Lithium-ion (Li-ion) cells are widely used for energy storage in various applications, including electric vehicles [1], renewable energy storage [3], aerospace [4], and consumer electronics [2] applications. High energy density and relatively long cycle life are among the primary advantages of Li-ion cells over other energy storage technologies [5]. However, Li-ion batteries are also prone to catastrophic failure driven by overheating. This phenomenon, often referred to as thermal runaway [6,7] involves the triggering of a series of exothermic decomposition reactions where heat generated in the cell increases exponentially with temperature. The positive feedback between heat generation and temperature [8] causes catastrophic cell failure, often involving fire and explosion. Understanding and addressing the risks associated with thermal runaway in Li-ion batteries is critical for ensuring safety and reliability of electrochemical energy storage devices [6,7].

In battery modules and packs, where many Li-ion cells are typically integrated, mitigating and preventing the propagation of thermal runaway from one cell to neighboring cells is critical. While the failure of a single cell within a sizable battery pack may be manageable, propagation of thermal runaway from a trigger cell to its neighboring cells and beyond can result in catastrophic failure of the entire battery pack. Various experimental investigations and modeling efforts have focused on techniques for mitigating thermal runaway propagation [9,10].

Large scale abuse testing, specifically for sensitivity analysis and system design, may be prohibitive due to the large number of design parameters. Therefore, developing robust numerical simulations can complement abuse experiments in accurate risk assessment and design. A wide range of models with various levels of complexity have been reported for thermal runaway simulation of a single Li-ion cell as well as battery packs. Various coupled, often non-linear physical phenomena have been modeled, including gas generation and pressure buildup [11], venting [12], particle ejection [13], and combustion of the vent gas [14]. These models range from lumped and thermal resistance networks [15,16] to detailed three-dimensional Computational Fluid Dynamics (CFD) models [17,18].

* Corresponding author at: 500 W First St, Rm 211, Arlington, TX 76019, USA.
E-mail address: jaina@uta.edu (A. Jain).

https://doi.org/10.1016/j.est.2025.117652
Received 6 February 2025; Received in revised form 29 April 2025; Accepted 3 July 2025
Available online 23 July 2025
2352-152X/© 2025 Elsevier Ltd. All rights are reserved, including those for text and data mining, AI training, and similar technologies.

Nomenclature

Symbol

A_{sei}	SEI decomposition frequency factor (s^{-1})
A_{ne}	Negative solvent frequency factor (s^{-1})
A_{pe}	Positive solvent frequency factor (s^{-1})
A_e	Electrolyte decomposition frequency factor (s^{-1})
$E_{a,sei}$	SEI decomposition activation energy ($Jmol^{-1}$)
$E_{a,ne}$	Negative solvent activation energy ($Jmol^{-1}$)
$E_{a,pe}$	Positive solvent activation energy ($Jmol^{-1}$)
$E_{a,e}$	Electrolyte decomposition activation energy ($Jmol^{-1}$)
C_{sei}	Carbon content in the SEI film
C_{sei0}	Initial value of C_{sei}
C_{ne}	Carbon content in the negative electrode
C_{ne0}	Initial value of C_{ne}
α	Dimensionless extent of reaction
α_0	Initial value of α
C_e	Proportion of the remaining electrolyte
C_{e0}	Initial value of C_e
m_{sei}	Reaction order for C_{sei}
m_{ne}	Reaction order for C_{ne}
m_{pe}	Reaction order for α
m_e	Reaction order for C_e
t_{sei}	Dimensionless thickness of the SEI film
$t_{sei,ref}$	Initial value of t_{sei}
H_{sei}	SEI decomposition heat release (Jg^{-1})
H_{ne}	Negative solvent heat release (Jg^{-1})
H_{pe}	Positive solvent heat release (Jg^{-1})
H_e	Electrolyte decomposition heat release (Jg^{-1})
W_c	Specific carbon content (gm^{-3})
W_p	Specific positive active material content (gm^{-3})
W_e	Specific electrolyte content (gm^{-3})

Acronyms

CFD	Computational Fluid Dynamics
LCO	Lithium Cobalt Oxide
NCA	Nickel Cobalt Aluminum Oxide
SEI	Solid Electrolyte Interphase
SOC	State Of Charge

One of the primary challenges associated with thermal runaway simulations is the high computational cost, especially for three-dimensional finite volume and finite element models. The nonlinear nature of equations that describe thermal runaway processes makes the simulations complex and computationally challenging. Additionally, rapid temperature rise during thermal runaway necessitates extremely small timesteps for convergence. Various techniques have been developed to optimize computational efficiency in thermal runaway simulations [19,20].

Previous studies have highlighted the importance of heat transfer through the interstitial material in determining the likelihood of thermal runaway propagation [7,9,10,21]. It has been shown that an intermediate thermal conductivity of the interstitial material may mitigate thermal runaway propagation for various abuse scenarios [21]. Extremely small thermal conductivities may facilitate the onset of thermal runaway in the trigger cell, even for small thermal excursions, by acting as an insulator and limiting heat dissipation. On the other hand, high thermal conductivity enhances heat transfer between cells, potentially aiding the propagation of thermal runaway if overall heat dissipation is inadequate.

The prevention and mitigation of thermal runaway is of much practical importance [7], and, therefore, has been addressed in a number of past papers. A number of thermal management techniques have been investigated towards this goal, including heat pipes [22], immersion cooling [23], liquid cooling [24] and phase change based cooling [25]. Design strategies such as placement of aerosol insulation [26] or metal spacers [27] between cells have also been proposed. Storing cells at low state of charge (SOC) has been reported to reduce the propensity of thermal runaway propagation [27]. Given the challenges associated with experimental measurements, there continues to remain a need for development of robust numerical simulation models to predict thermal runaway propagation and comparison of such simulation tools with experimental measurements. Specifically, there is a lack of past work on, and, therefore, a need for simulations to help understand the potential role of phase transition materials in thermal management and thermal runaway prevention in battery packs. In particular, it is important to understand the role of thermal properties of the phase transition material in preventing thermal runaway propagation.

This work presents a numerical simulation of a battery pack in order to predict the onset and propagation of thermal runaway in response to a thermal abuse scenario. The numerical simulation is developed to investigate thermal runaway propagation in a 5 by 5 Li-ion battery pack configuration, corresponding to an experimental abuse test carried out. In both the experiment and simulation, the gap between cells contains a block-type phase transition material. Characteristics of the phase transition material used in the battery pack are measured. A comparison between experimental data and simulation results is presented. Results indicate that the thermal conductivity of the interstitial material plays a critical role in determining thermal runaway propagation.

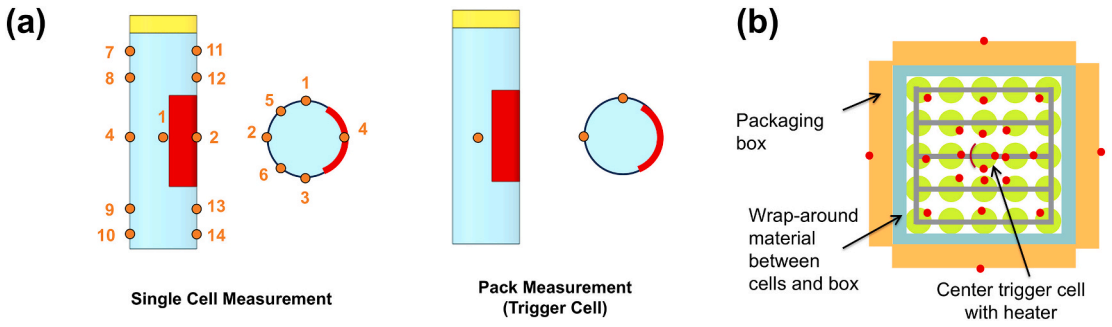

Fig. 1. (a) Thermocouple locations on trigger cell for single-cell and pack measurements, (b) Schematic of the experimental setup showing a 5 by 5 array of cells, with a heater around the center trigger cell. Circles indicate locations of thermocouples.



Fig. 2. Pictures of the battery pack before and after the test.

2. Experimental measurements

2.1. Experimental data for model validation

2.1.1. Single-cell measurements

The experimental data used for validation of the simulation model developed in the present work are obtained from unpublished experiments conducted by Electrochemical Safety Research Institute at UL Research Institutes (ULRI/ESRI). In brief, the thermal runaway test is carried out on an 18650 Nickel Cobalt Aluminum Oxide (NCA) cell instrumented with 25.4 mm by 25.4 mm heating tape and fourteen K-type thermocouples at various heights and circumferential locations, as shown in Fig. 1(a). The results from the tests are used for model calibration and parameter optimization discussed in detail in the next section. Having several thermocouples at different axial and circumferential locations helps identify and optimize cell thermal conductivities in the axial, radial, and circumferential directions. The test article is then placed in a chamber. The Li-ion cell is heated up at 10 °C/min until the cell went into thermal runaway. The heating power, cell temperature at various locations, and the cell voltage are measured and recorded as functions of time.

2.1.2. Pack-level measurements

Similarly, the numerical simulation developed in this study is compared with unpublished experimental data obtained from a 5 by 5 pack-level abuse test carried out by ULRI/ESRI. Fig. 1(b) presents a schematic of the experimental setup. The experiment involves testing new 18650 format Li-ion cells at 100% SOC. The Li-ion cells are electrically connected in parallel (25P) in a 5 by 5 configuration and placed inside a block-type interstitial material with a phase transition temperature of 122 °C. Based on the intent of the abuse test to study thermal runaway propagation for shipping applications, the entire test article is placed inside a shipping box with the dimensions of 130 cm by 130 cm by 95 cm, as shown schematically in Fig. 1(b). To initiate thermal runaway, a 40 W tape heater is used to heat the center cell to achieve a heating rate of 10 °C/min until the trigger cell entered thermal runaway or reached a temperature of 200 °C. A number of thermocouples are placed for temperature measurement, as indicated in Fig. 1(b). Fig. 2 shows top view pictures of the test article before and after the experiment.

2.2. Measurement of thermal properties of phase transition material

Thermal properties of the phase transition material are measured using the laser flash method in a Netzsch LFA467 instrument. The phase transition material used in this test is provided by ULRI. The material was used in their test series, the results for which are still unpublished. Samples of 6 mm diameter and 1.0 mm thickness are prepared. One face of the sample is flashed with an energy pulse from a laser source, while the temperature on the other face is measured using an infrared detector. Temperature measured on the other face as a function of time is compared with the standard Cape-Lehman model with pulse length correction to determine the thermal diffusivity of the sample. Further, the peak temperature for the sample is compared with that of a standard material with well-known thermal properties to determine the heat capacity of the phase transition material. These measurements, along with separate measurements of density provide sufficient information to determine the thermal conductivity of the material. All measurements are carried out at room temperature and repeated three times. Thermophysical property data for the phase transition material and other materials in the battery pack are summarized in Table 1 [28,29].

Table 1
Thermophysical properties of materials used in numerical simulations [28,29].

Material	Thermophysical properties		
	Thermal conductivity ($Wm^{-1}K^{-1}$)	Density (kgm^{-3})	Specific heat capacity ($kJkg^{-1}K^{-1}$)
Li-ion cell	0.2, 32, 32 (r, θ, z)	2280	0.715
Phase transition material	0.65	700	2.0
Metal heater	202.4	2800	0.87
Tab material	91	8900	0.460

3. Numerical simulations

Numerical simulations are carried out in a finite-volume framework implemented in ANSYS Fluent software. Sub-sections below describe various aspects of the simulation set up.

3.1. Battery pack geometry

A pack of twenty-five NCA cells of 18650 form factor (18 mm diameter and 65.0 mm height) arranged in a 5 by 5 array that mimics the experimental work carried out at ULRI/ESRI, is considered in this work. A schematic of the half-symmetry model of the pack is shown in Fig. 3 (a). A constant cell-to-cell gap of 2 mm is considered. Cells are electrically interconnected to each other in a 25P configuration using 0.13 mm thick and 6.4 mm wide Nickel tabs, as shown in the top view in Fig. 3(b). The region between cells is occupied by a phase transition material that undergoes phase transition and thus absorbs heat in a known temperature range. The phase transition process is weaker than a full phase change, such as melting, but keeps the structural integrity of the interstitial material intact. Thermal runaway is caused by external heating in a heating tape wrapped around the center cell (cell number 13). The geometry and location of the heating tape correspond to experimental conditions, as shown schematically in Fig. 1(b).

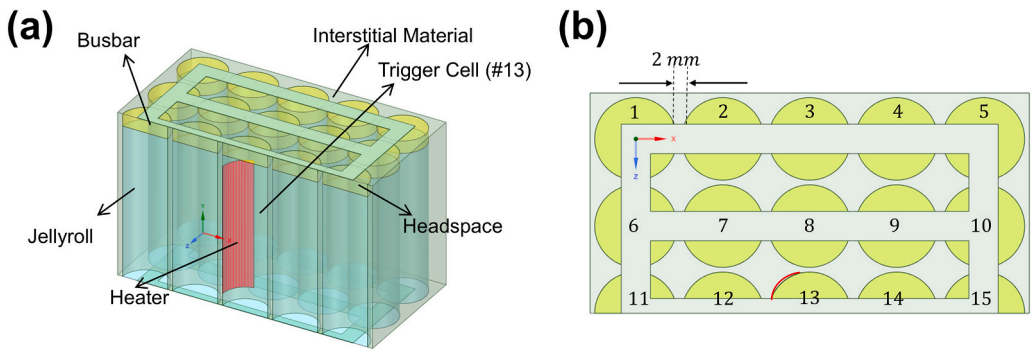

Fig. 3. Schematic of the half-symmetry simulation geometry: (a) The entire battery pack, showing various geometrical features, (b) Top view showing the various cells in the pack, including the trigger cell #13.

Table 2
Summary of non-linear heat generation reactions responsible for thermal runaway [6,7].

Reaction	Heat generation	Rate of reaction
SEI decomposition (sei)	$Q_{sei} = H_{sei} W_c R_{sei}$	$R_{sei} = A_{sei} exp\left[\frac{-E_{a,nsei}}{R_u T}\right] C_{sei}^m$
		$\frac{dC_{sei}}{dt} = -R_{sei}$
Negative-solvent reaction (ne)	$Q_{ne} = H_{ne} W_n R_{ne}$	$R_{ne} = A_{ne}\left[\frac{-t_{sei}}{t_{sei,ref}}\right] \exp\left[\frac{-E_{a,ne}}{R_u T}\right] C_{ne}^m$
		$\frac{dC_{ne}}{dt} = -R_{ne}$
Positive-solvent reaction (pe)	$Q_{pe} = H_{pe} W_p R_{pe}$	$R_{pe} = A_{pe} \alpha^{m,pe} (1-\alpha)^{m,pe} \exp\left[\frac{-E_{a,pe}}{R_u T}\right]$
		$\frac{d\alpha}{dt} = -R_{pe}$
Electrolyte decomposition (e)	$Q_e = H_e W_e R_e$	$R_e = A_e \exp\left[\frac{-E_{a,e}}{R_u T}\right] C_e^m$
		$\frac{dC_e}{dt} = -R_e$

3.2. Simulation details

The geometry described in Section 3.1 is modeled and discretized in ANSYS Fluent that uses the finite volume technique. Polyhedral meshing is used in order to improve the quality of the mesh. Localized mesh refinement is used in and around the heater and Nickel tabs to generate a locally dense mesh with a sufficient number of elements. Grid- and timestep-sensitivity analysis is carried out in order to ensure sufficiently fine discretization in space and time so that results remain independent of further refinement. A final mesh with around 4 million elements and a timestep of 1 s is used for all simulations. Whenever possible, symmetry planes are used to reduce the computational domain and improve the computational time. In particular, half-symmetry is used in pack-level thermal simulations.

3.3. Heat generation model

At elevated temperatures, heat generation in the cell is commonly linked to the chemical decomposition of its components. The heat produced by each decomposition reaction is directly proportional to its reaction rate, often represented as Arrhenius reactions. Four decomposition reactions have been reported in the literature, mainly for Lithium Cobalt Oxide (LCO) cells [30,31]. These reactions encompass the decomposition of the solid-electrolyte interphase (SEI) layer on the anode surface, the reaction of anode active material with the electrolyte solvent, the reaction of cathode active material with the electrolyte solvent, and the electrolyte decomposition reaction. This study implements similar exothermic decomposition reactions. Table 2 summarizes the reaction rates and the heat generation terms implemented as volumetric heat sources in the energy conservation equation for each cell [6,7]. Note that in Table 2, t_{SEI} refers to the normalized value of the SEI thickness which represents the Lithium content in the SEI. $t_{SEI,ref} = 0.033$ is a reference value for the SEI thickness [30]. The t_{SEI} term appears in the equation for the negative-solvent reaction, and not for the positive-solvent reaction, because the SEI is formed primarily on the negative electrode, and not the positive electrode. Further, α in the positive-solvent reaction refers to the degree of conversion, with an initial value of 0.04, based on past literature [30]. As the reaction proceeds, the value of α increases, based on its governing differential equation listed in Table 2.

Note that phase change processes within the cell, such as evaporation of the electrolyte or melting of the separator are not explicitly modeled in this work. The enthalpy of such processes is likely to be much smaller than those of the four major decomposition reactions, which have been modeled in detail in this work using Arrhenius chemistry. This approximation helps focus on heat transfer and thermal runaway at the larger spatial scale of the battery pack, while dominant processes at the small spatial scale within the cell are represented by the Arrhenius parameters. Further, it is assumed that the phase transition material does not fully melt, and, therefore, natural convection heat transfer in the liquid has been neglected.

3.4. Governing equations for thermal conduction

Due to the well-known anisotropy of thermal conduction in Li-ion cells, the following transient energy conservation equation is modeled for each cell:

$$\frac{1}{r}\frac{\partial}{\partial r}\left(k_r r \frac{\partial T}{\partial r}\right) + \frac{k_\theta}{r^2}\frac{\partial^2 T}{\partial \theta^2} + k_z \frac{\partial^2 T}{\partial z^2} + q''' = \rho c_p \frac{\partial T}{\partial t} \quad (1)$$

Table 3
Values of key heat generation parameters for decomposition reactions obtained from parameter optimization discussed in Section 3.6. In addition, $t_{SEI,ref} = 0.03$ and $\alpha_0 = 0.04$.

Reaction	A, Frequency factor (s^{-1})	E_a, Activation energy ($kJkmol^{-1}$)	H, Heat release (J)	Initial value	m, Reaction order	W, Specific material content (gm^{-3})
SEI decomposition (sei)	45.6	35,701	54.83	0.15	1	714,020
Negative solvent decomposition (ne)	2.480×10^{13}	111,930	3000	0.75	1	714,020
Positive solvent decomposition (pe)	6.667×10^{11}	127,007	600	1.0	1	1,114,200
Electrolyte decomposition (e)	5.140×10^{25}	274,000	155	1.0	1	261,550

where q''' is the source term originating from the heat generation reactions discussed in the previous sections.

In contrast with cells, thermal conduction in all other materials in the simulation, including the heating tape, Nickel tabs, and the box material is isotropic in nature. Standard thermal properties of metal heater and Nickel tables [29] are used, as summarized in Table 1. All thermal properties are assumed to be independent of temperature. A uniform convective heat transfer coefficient of 16 $Wm^{-2}\ K^{-1}$ is applied on the outer surfaces of the geometry to model natural convective heat loss to the surroundings. The entire battery pack is assumed to be at room temperature initially.

3.5. Phase transition modeling

The interstitial material between cells in the present work undergoes solid-to-solid phase transition in a specific temperature range. Phase transition is of particular interest because the associated latent heat may be able to absorb significant thermal energy in the temperature range of phase transition. Moreover, unlike solid-to-liquid phase change, such phase transition does not produce a liquid, which can be complicated to handle in a realistic battery pack. Thermal conduction in the phase transition material is assumed to be governed by a constant isotropic thermal conductivity, the value of which is determined through measurements described previously. Heat absorbed during phase transition is modeled by a temperature-dependent heat capacity that accounts for the latent heat of phase transition as an additional contribution to heat capacity. The phase transition temperature is measured experimentally. Moreover, the latent heat of phase transition is estimated by the experimentally measured time taken for the material to undergo phase transition.

3.6. Parameter optimization

This study simulates an abuse test of a pack of NCA cells. The original values of the heat of reactions and kinetic parameters, such as activation energies and frequency factors, were initially reported for LCO cells. A parameter optimization technique is used to calibrate the four decomposition reactions for the current simulation. The parameter optimization is conducted to align these parameters with the experimental data obtained from the previous abuse test of a single NCA cell, where the surface of the cell is instrumented with an array of thermocouples at various axial and circumferential locations. The optimization method used here has been reported in a previous study [32], where a validation against full-scale numerical simulations [12] was also reported. For optimization, a simplified 3D thermal resistance network model is developed in GT_SUITE v2024 software. The model includes thermal components with internal thermal resistances in radial, axial, and circumferential directions to represent conduction heat transfer. Each thermal component comprises a lumped mass and one or more thermal resistances to facilitate heat conduction to/from the component. The spatial resolution is improved by dividing the Li-ion cell into multiple thermal components connected in each direction, making it similar to a 3D finite volume model. The reason for using a more simplified thermal model for optimization is the computational efficiency of such models. A built-in design optimizer tool based on an accelerated genetic algorithm with a transient targeting optimization mode is utilized to calibrate cell thermal properties and the kinetic parameters based on the transient output of the thermal simulation and the experimental data as a function of time. The optimization is carried out in two stages, i.e., pre-heating and self-heating. The pre-heating stage is optimized to calibrate the specific heat capacity of the cell. The self-heating stage is optimized to calibrate the frequency factors, activation energies, and the heat of reactions. The optimized parameters are summarized in Table 3.

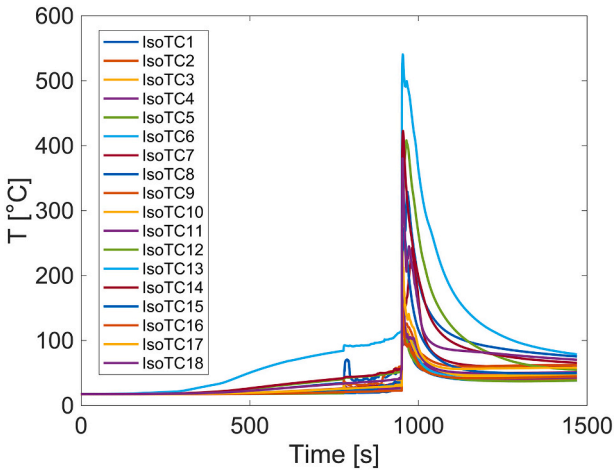

Fig. 4. Representative measurements of temperatures of various thermocouples as functions of time.

4. Results and discussion

4.1. Experimental measurements

The experimental results used in this simulation are obtained from ULRI/ESRI. The results of the large study are unpublished, therefore, only the relevant data plots for the current simulation study have been replicated in the present work. Fig. 4 presents representative plots of thermocouple measured temperature of various cells as functions of time in the 5 by 5 pack-level experiment based on the unpublished experimental dataset. These data show gradual increase in temperature initially, which is mostly limited to the trigger cell. However, once the trigger cell enters thermal runaway, a very rapid propagation of thermal runaway to other cells in the pack is observed. Once the thermal runaway process is complete, all cells cool down gradually. Note that based on manufacturer specifications, an uncertainty of up to 2.2 % is expected in the temperature measurements, which corresponds to around 12 °C at the peak temperature shown in Fig. 4.

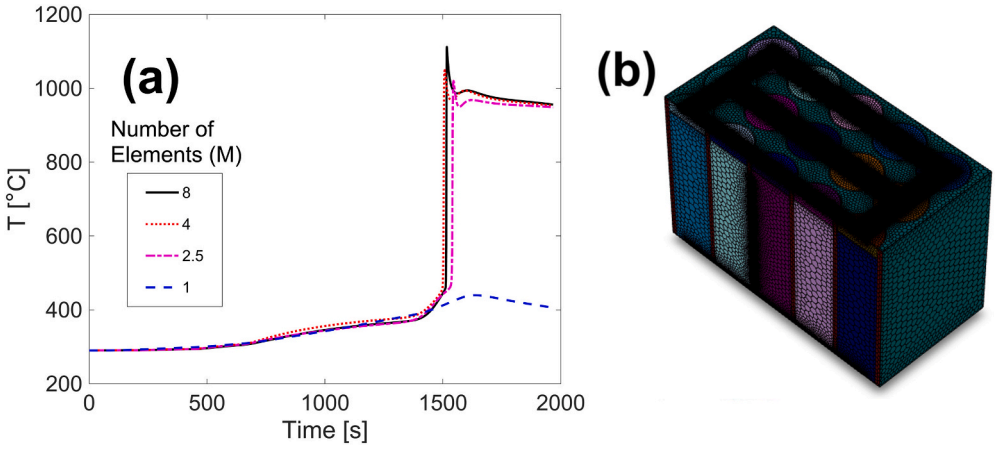

Fig. 5. Grid independence verification: Temperature at the top surface of the trigger cell as a function of time for multiple values of number of elements.

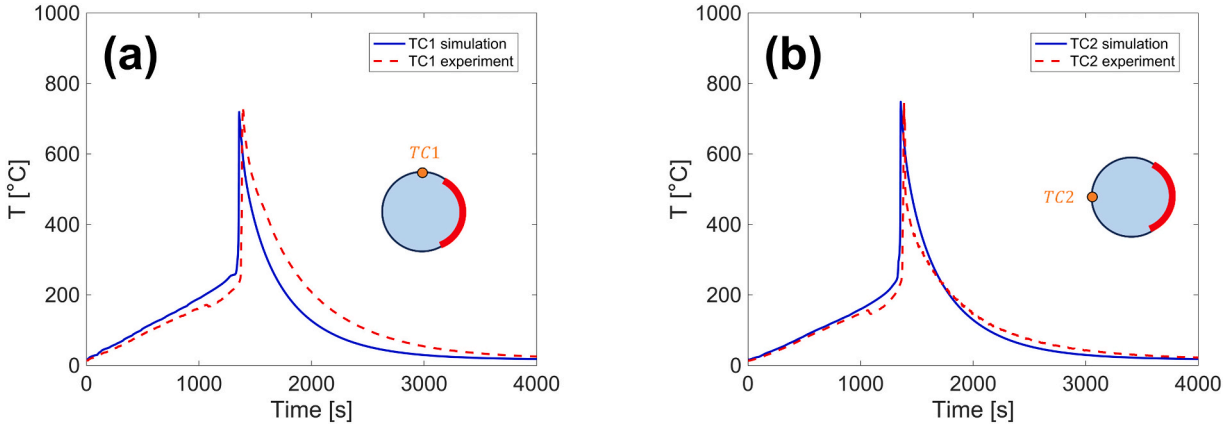

Fig. 6. Single-cell comparison with experiments: Temperature at three circumferential locations around the cell at half-height prior to and after thermal runaway.

4.2. Grid independence of simulations

Fig. 5(a) presents a plot of temperature at the center of the bottom surface of the cell as a function of time for four different number of elements in the pack-level simulation. It is found that for a relatively small number of elements (1 million), the simulation fails to predict the onset of thermal runaway that is observed in the experiments. With increasing number of elements, the results become more realistic, including a very sharp increase in temperature at the onset of thermal runaway, followed by a peak and then a slow reduction in temperature once reactants are consumed. Results also become stable once the number of elements is sufficiently large. Between 4 million and 8 million elements, the change in the temperature curve is negligible. This indicates that the use of at least 4 million elements is required to ensure grid independence of the simulation results. Therefore, all subsequent simulations presented here use at least 4 million elements. The significant computational cost of 4 million elements in each cell mainly stems from the strong non-linearity in the underlying physics of this problem. Fig. 5(b) presents a picture of the final mesh used for all subsequent simulations.

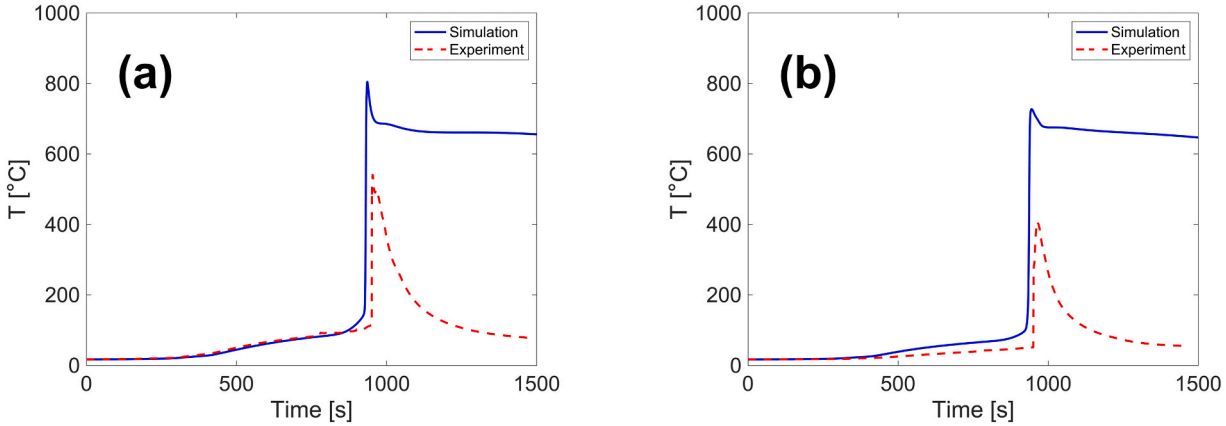

Fig. 7. Pack-level comparison with experiments: (a) Temperature at the bottom faces of trigger and (b) neighboring cell prior to and after thermal runaway.

Table 4
Values of baseline thermophysical properties of the interstitial material used for parametric analysis.

Thermophysical property	Value
Thermal conductivity	0.65 ($Wm^{-1}K^{-1}$)
Heat capacity	2000 ($Jkg^{-1}K^{-1}$)
Latent heat of phase transition	15,000 (Jkg^{-1})
Phase transition temperature range	110–130 (°C)

4.3. Single-cell simulation

Before simulating thermal runaway and propagation in the battery pack, a single-cell simulation is conducted to compare with experimental data. The single-cell simulation uses parameters calibrated using the reduce-order model described in Section 3.6. Comparison with experimental measurements is shown in Fig. 6. Figs. 6(a) and 6(b) presents temperature plots as a function of time for thermocouples TC1 and TC2 attached to the outer surface of the cell, as shown in Fig. 1. Thermocouple locations relative to the heater orientation are shown in the insets of Figs. 6(a) and 6(b). Both experimental data and simulation results are presented. Simulation results show that the calibrated parameters using a 3D thermal resistance network model result in good agreement with the experimental data when implemented in the 3D CFD model. As expected, thermocouple 1, located closer to the heater, exhibits a larger temperature rise than thermocouple 2 for both experimental measurements and simulations. However, the difference between the two is not significant, which is likely due to the relatively large circumferential thermal conductivity due to good thermal conduction around the cell casing.

It is important to note that the experimental data show a characteristic temperature drop at around 1000 s due to the activation of the vent mechanism, which allows for the hot gases within the cell to escape as well as the electrolyte evaporation. Previous studies accounted for this cooling phenomenon in the numerical simulation by introducing a two-stage electrolyte evaporation mechanism [33]. The vent activation mechanism and, consequently, the cooling effect due to the hot gas release and electrolyte evaporation are not considered in the simulation model. Instead, the focus of the model calibration process is more on capturing the correct initial heating rate, time to thermal runaway, and the cooling stage. The numerical simulation correctly captures the time at which thermal runaway occurs, as well as the peak temperature. The numerical simulation model also captures the temperature decay curve following the completion of thermal runaway with reasonable accuracy.

There may be several potential sources of error, on both experimental and simulation sides, that may contribute to the minor disagreement between the two. The accuracy of experimental measurements depends strongly on the capability of the thermocouples to continue to accurately measure temperature in the hostile thermal runaway period. On the numerical simulations side, uncertainties in the values of key simulation parameters, such as activation energy, may strongly influence temperature prediction accuracy. Moreover, values of the thermophysical properties of the cell, including thermal conductivity and specific heat capacity have been optimized using a 3D thermal resistant network model with limited spatial resolution compared to the CFD model.

4.4. Pack-level comparison with experimental measurements

A thermal simulation of the 5 by 5 battery pack shown in Fig. 3 is carried out. Consistent with experiments carried out at ULRI/ESRI, the center cell is chosen as the trigger cell. A comparison between numerical simulations and experimental data for the trigger cell (cell 13) and its immediate neighboring cell (cell 12) is shown in Figs. 7(a) and 7(b), respectively. Results show that the model is able to accurately capture the initial heating stage. The simulations and measurements are in close agreement in terms of the time at which the trigger cell goes into thermal runaway, as well as the steep rate of temperature change during thermal runaway. The peak temperature calculated by the simulation is somewhat higher than that from measurements. A potential reason behind this is radiative heat loss from the top and bottom surfaces of the cell, particularly at elevated temperature. Further, it is possible that thermocouples in experiments are not able to accurately track the very large rate of temperature change during thermal runaway.

4.5. Parametric analysis of key thermophysical properties

It is pertinent to utilize the numerical simulation model developed in this work to understand the impact of key thermophysical properties and parameters on thermal runaway response in a battery pack. Such insights may be valuable for battery pack design by guiding the search for phase transition materials that may be appropriate for preventing thermal runaway in Li-ion battery packs. Key thermophysical properties of interest include thermal conductivity, heat capacity, latent heat, and the temperature range in which such phase transition occurs in the case of a phase transition material. To carry out this parameter analysis systematically, a baseline set of parameter values of these properties is chosen, as summarized in Table 4. The effect of varying one parameter at a time on thermal runaway characteristics is studied while holding three parameters constant at values listed in Table 4.

Fig. 8 presents plots of trigger cell surface temperature as a function of time for multiple values of thermal conductivity of the interstitial material, including $k = 0.03$ Wm^{-1} K^{-1}, which corresponds to air. It is

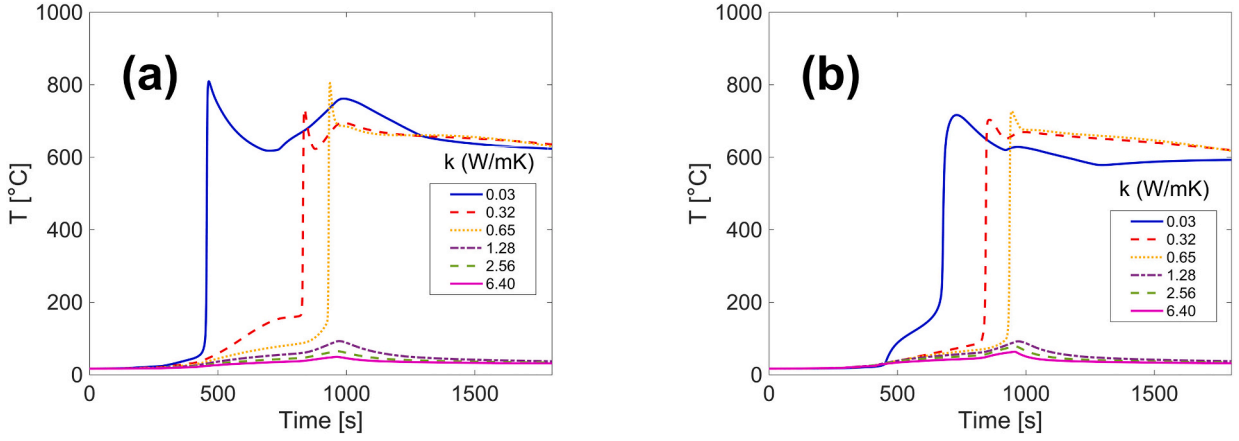

Fig. 8. Temperature at the bottom faces of the (a) trigger and (b) neighboring cells as functions of time for five different values of the interstitial material thermal conductivity.

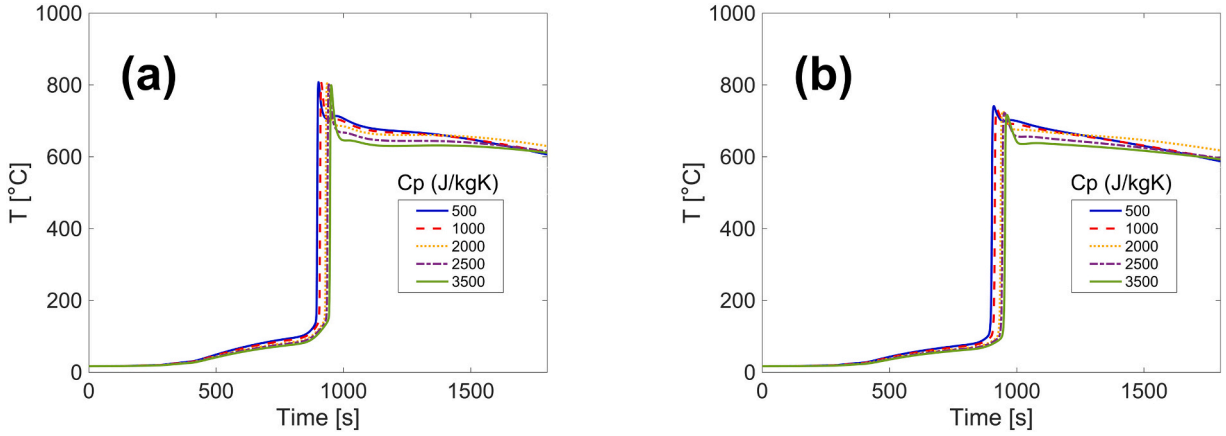

Fig. 9. Temperature at the bottom faces of the (a) trigger and (b) neighboring cells as functions of time for five different values of the interstitial material heat capacity.

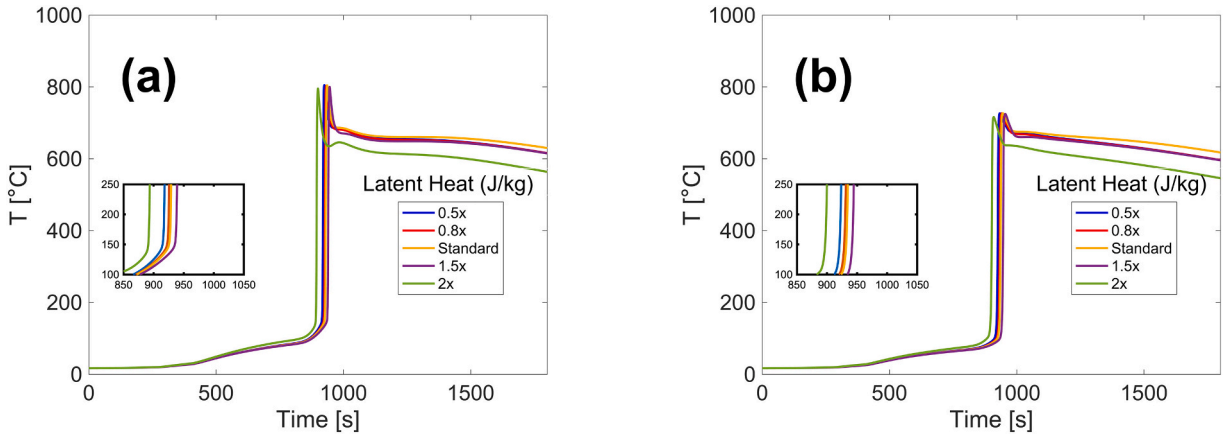

Fig. 10. Temperature at the bottom faces of the (a) trigger and (b) neighboring cells as functions of time for five different values of the interstitial material latent heat.

found that reducing the thermal conductivity of the interstitial material results in earlier occurrence of thermal runaway. Compared to the standard thermal conductivity used in this work, setting the thermal conductivity to that of air results in thermal runaway occurring in less than half the time, and also with a greater temperature peak. This is mainly because reducing thermal conductivity of the interstitial material results in significantly increased impedance to heat removal from the trigger cell. Such a pileup of heat within the cell feeds the positive feedback loop between temperature rise and heat generation, thereby resulting in faster approach towards thermal runaway. When thermal conductivity is sufficiently large, for example, curves corresponding to $k = 1.28$ Wm^{-1} K^{-1} and larger in Fig. 7, there is sufficient thermal dissipation, and temperature rise in the trigger cell is not large enough to result in thermal runaway. In such cases, there is neither onset (Fig. 8(a)) nor propagation (Fig. 8(b)) of thermal runaway. Note that in each of the three cases shown in Fig. 8(a) that result in thermal runaway, the trigger cell temperature experiences a secondary peak, which is due to thermal energy received by the trigger cell from the thermal runaway event in the neighboring cells. This is confirmed by the close match between the time at which temperature begins to rise in such cases in Fig. 8(a) and the time at which thermal runaway starts in the neighboring cells, as shown in Fig. 8(b).

Under the specific conditions studied here, Fig. 8 indicates that the thermal conductivity threshold at which thermal runaway onset no longer occurs is between 0.64 and 1.28 Wm^{-1} K^{-1}. These are not particularly large values, and several common engineering materials may be able to offer such thermal conductivity.

The effect of heat capacity on thermal runaway characteristics is analyzed next. Similar to Fig. 8, the trigger and neighboring cell surface temperatures are plotted in Figs. 9(a) and 9(b), respectively, for multiple values of heat capacity, including the baseline value listed in Table 4, as well as two values below and two values above the baseline. Fig. 9 indicates that while increasing heat capacity does delay the onset of thermal runaway somewhat, the effect is much weaker than that of thermal conductivity presented before. The increased time of thermal runaway with increasing heat capacity is mainly because a larger heat capacity, by definition, results in reduced rate of temperature rise, which limits temperature-driven heat generation and eventually thermal runaway. Within reasonable values of heat capacity, however, the impact is quite minor, likely because the highly non-linear heat generation process in this case dominates over sensible temperature rise that is governed by the heat capacity.

An interesting aspect of Fig. 9 is that at a sufficiently large heat capacity, 3500 Jkg^{-1} K^{-1} in this case, there is no longer any thermal runaway due to the reduced temperature rise. However, note that this is a rather large value of heat capacity that is unlikely to be available with practical engineering materials. Heat capacity of most metals is less than 1000 Jkg^{-1} K^{-1}, and while some polymers may offer heat capacity of around 2000 Jkg^{-1} K^{-1}, such materials also exhibit much poorer thermal conductivity, which, Fig. 8 indicates has a more dominant impact on thermal runaway characteristics. A combination of high thermal conductivity and high heat capacity is, in general, difficult to obtain in

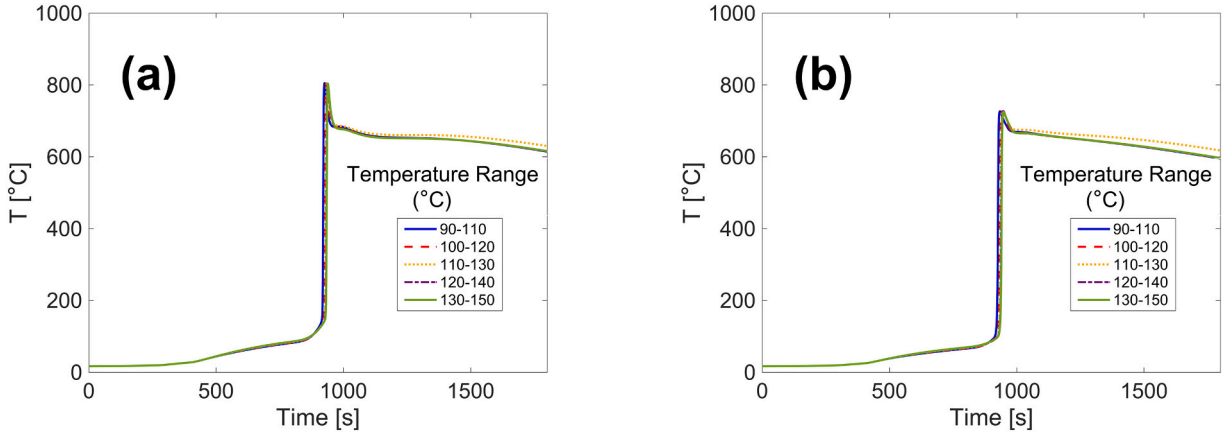

Fig. 11. Temperature at the bottom faces of the (a) trigger and (b) neighboring cells as functions of time for five different values of the interstitial phase transition temperature.

practical materials.

Together, Figs. 8 and 9 indicate that the search for appropriate interstitial materials for Li-ion battery packs must focus on higher thermal conductivity than higher heat capacity. This is consistent with past work [21] that has also identified thermal conductivity as an important thermal property for preventing thermal runaway propagation, as well as the general understanding of the important role played by thermal conductivity in heat transfer in phase change materials.

The effect of two parameters associated with the phase transition process – latent heat and phase transition temperature – on thermal runaway characteristics is presented next. Figs. 10(a) and 10(b) plots temperatures of the trigger and neighboring cells, respectively, as functions of time for multiple values of the latent heat of the interstitial material. Curves corresponding to the baseline values and several others below and above the baseline are plotted. Insets show the very large rate of temperature rise around the time of onset of thermal runaway. It is found that changing the latent heat does not significantly change the predicted nature of thermal runaway onset and propagation in the battery pack. There is a minor increase in the time of occurrence of thermal runaway by increasing the latent heat, which is likely due to a greater rate of heat absorption in the interstitial material. Nevertheless, the curves are relatively closely spaced, and onset and propagation of thermal runaway is predicted for each case.

A similar investigation of the impact of the phase transition temperature range is carried out. Results are presented in Figs. 11(a) and 11(b) for the trigger and neighboring cells, respectively. Similar to the latent heat, it is found that the temperature range of phase transition has only a weak impact on the nature of the onset and propagation of thermal runaway.

In summary, the parametric investigation of the effect of thermal properties of the phase transition material shows that thermal conductivity has, by far, the strongest influence on thermal runaway characteristics.

5. Conclusions

Developing a fundamental understanding of thermal runaway propagation in a battery pack is of much practical importance in designing safe and reliable energy storage and conversion systems. The key novelty of the present work is in developing a numerical simulation tool to predict thermal runaway propagation and comparing with experimental measurements. Additionally, this work offers useful insights into the use of a phase transition material in the battery pack for improving thermal performance. Key insights gained from this work include the importance of thermal conductivity as the key thermophysical property that governs the onset and propagation of thermal runaway in the battery pack.

It is important to recognize a few key limitations of the simulations approach used in this work. Venting and combustion of volatile gases outside the cells is not explicitly modeled. Doing so typically requires a detailed modeling of species transport and chemical reactions. Similarly, radiative heat transfer has not been modeled explicitly, which may be justified because the presence of the phase transition material between cells precludes the possibility of radiative heat exchange between cells. Finally, all thermal properties are assumed to be temperature-independent, which may introduce a small error when the temperature rise is significantly large.

The results discussed in this work may have direct relevance in the broader context of battery safety and thermal management of energy storage systems. There is an ongoing need for effective techniques for heat removal and thermal management of batteries, not only to improve performance but also to address safety challenges such as thermal runaway. Performance analysis of a phase transition interstitial material presented here may directly contribute towards this goal. Specifically, results related to the sensitivity of thermal runaway onset and propagation to thermophysical properties of the phase transition material may contribute towards materials development as well as practical implementation in realistic battery packs. While not addressed directly in this work, optimization of thermal runaway simulations remains an important challenge in computational research on thermal runaway in Li-ion cells. Due to the extremely large rate of heat generation, and, therefore, rate of temperature rise around the onset of thermal runaway, numerical simulations typically slow down dramatically in order to stay within required tolerance levels. Development of techniques to reduce the computational time, even if at a reasonable cost of reduced accuracy, may be important for development of practical predictive tools for thermal runaway. This is identified as an important future work in this direction.

CRediT authorship contribution statement

Muhammad Mehdi Abbas: Writing – review & editing, Formal analysis, Methodology, Writing – original draft, Investigation, Data curation, Visualization. **Dhananjay Mishra:** Writing – review & editing, Investigation, Writing – original draft, Formal analysis, Methodology. **Emad Hasrati:** Writing – original draft, Visualization, Investigation, Writing – review & editing. **Byoungchul Kwon:** Writing – review & editing, Investigation, Writing – original draft, Visualization. **Vinay Premnath:** Visualization, Writing – original draft, Writing – review & editing, Investigation. **Judith Jeevarajan:** Writing – original draft, Conceptualization, Methodology, Formal analysis, Writing – review & editing, Project administration, Supervision. **Ankur Jain:** Writing –

review & editing, Formal analysis, Writing – original draft, Methodology, Supervision, Project administration, Conceptualization.

Declaration of competing interest

The authors declare that they have no known competing financial interests or personal relationships that could have appeared to influence the work reported in this paper.

Acknowledgments

The authors would like to acknowledge funding from UL Research Institutes (ULRI).

Data availability

Data will be made available on request.

References

[1] M.A. Hannan, M.M. Hoque, A. Hussain, Y. Yusof, P.J. Ker, State-of-the-art and energy management system of lithium-ion batteries in electric vehicle applications: Issues and recommendations, IEEE Access 6 (2018) 19362–19378, https://doi.org/10.1109/ACCESS.2018.2817655.
[2] B. Diouf, R. Pode, Potential of lithium-ion batteries in renewable energy, Renew. Energy 76 (2015) 375–380, https://doi.org/10.1016/j.renene.2014.11.058.
[3] J.P. Fellner, G.J. Loeber, S.P. Vukson, C.A. Riepenhoff, Lithium-ion testing for spacecraft applications, J. Power Sources 119 (2003) 911–913, https://doi.org/10.1016/S0378-7753(03)00222-2.
[4] R.J. Brodd, Recent developments in batteries for portable consumer electronics applications, Electrochem. Soc. Interface 8 (3) (1999) 20, https://doi.org/10.1149/2.F05993IF.
[5] K.W. Beard, T. Reddy, Linden's Handbook of Batteries, 5th ed., McGraw Hill, 2019.
[6] T.M. Bandhauer, S. Garimella, T.F. Fuller, A critical review of thermal issues in lithium-ion batteries, J. Electrochem. Soc. 158 (2011) R1–R25, https://doi.org/10.1149/1.3515880.
[7] D. Mishra, E. Hasrati, A. Jain, Thermal management of Li-ion cells for improved safety and performance: a review, Annu. Rev. Heat Transf. 26 (2023) 131–176, https://doi.org/10.1615/AnnualRevHeatTransfer.2023048989.
[8] A. Jain, M. Parhizi, L. Zhou, G. Krishnan, Imaginary eigenvalues in multilayer one-dimensional thermal conduction problem with linear temperature-dependent heat generation, Int. J. Heat Mass Transf. 170 (2021), https://doi.org/10.1016/j.ijheatmasstransfer.2021.120993 (pp. 120993:1-10).
[9] S. Shahid, M. Agelin-Chaab, A review of thermal runaway prevention and mitigation strategies for lithium-ion batteries, Energy Convers. Manag. X 16 (2022) 100310, https://doi.org/10.1016/j.ecmx.2022.100310.
[10] B. Xu, J. Lee, D. Kwon, L. Kong, M. Pecht, Mitigation strategies for Li-ion battery thermal runaway: a review, Renew. Sust. Energ. Rev. 150 (2021) 111437, https://doi.org/10.1016/j.rser.2021.111437.
[11] R. Zhao, Z. Lai, W. Li, M. Ye, S. Yu, Development of a coupled model of heat generation and jet flow of lithium-ion batteries during thermal runaway, J. Energy Storage 63 (2023) 107048, https://doi.org/10.1016/j.est.2023.107048.
[12] J.K. Ostanek, M. Parhizi, W. Li, G. Kilaz, K.R. Crompton, CFD-based thermal abuse simulations including gas generation and venting of an 18650 Li-ion battery cell, J. Electrochem. Soc. 170 (2023) 090512, https://doi.org/10.1149/1945-7111/acf4c1.
[13] P. Zhang, J. Lu, K. Yang, H. Chen, Y. Huang, A 3D simulation model of thermal runaway in Li-ion batteries coupled particles ejection and jet flow, J. Power Sources 580 (2023) 233357, https://doi.org/10.1016/j.jpowsour.2023.233357.
[14] D. Mishra, P. Zhao, A. Jain, Thermal runaway propagation in Li-ion battery packs due to combustion of vent gases, J. Electrochem. Soc. 169 (2022), https://doi.org/10.1149/1945-7111/ac91a7 (100520: 1–10);
D. Kong, G. Wang, P. Ping, J. Wen, A coupled conjugate heat transfer and CFD model for the thermal runaway evolution and jet fire of 18650 lithium-ion battery under thermal abuse, E-transportation 12 (2022) 100157, https://doi.org/10.1016/j.etran.2022.100157.
[15] G. Wang, P. Ping, R. Peng, H. Lv, H. Zhao, W. Gao, D. Kong, A semi reduced-order model for multi-scale simulation of fire propagation of lithium-ion batteries in energy storage system, Renew. Sust. Energ. Rev. 186 (2023) 113672, https://doi.org/10.1016/j.rser.2023.113672.
[16] X. Feng, X. He, M. Ouyang, L. Lu, P. Wu, C. Kulp, S. Prasser, Thermal runaway propagation model for designing a safer battery pack with 25 ah $LiNi_xCo_yMn_zO_2$ large format lithium ion battery, Appl. Energy 154 (2015) 74–91, https://doi.org/10.1016/j.apenergy.2015.04.118.
[17] G. Wang, P. Ping, Y. Zhang, H. Zhao, H. Lv, X. Gao, W. Gao, D. Kong, Modeling thermal runaway propagation of lithium-ion batteries under impacts of ceiling jet fire, Process Saf. Environ. Prot. 175 (2023) 524–540, https://doi.org/10.1016/j.psep.2023.05.047.
[18] D. Mishra, R. Tummala, A. Jain, Investigation of propagation of thermal runaway during large-scale storage and transportation of Li-ion batteries, J. Energy Storage 72B (2023), https://doi.org/10.1016/j.est.2023.108315 (pp. 108315: 1–11).
[19] J. Ostanek, M. Parhizi, J. Jeevarajan, A novel method for alleviating numerical stiffness in Li-ion thermal abuse models, J. Power Sources Adv. 23 (2023) 100123, https://doi.org/10.1016/j.powera.2023.100123.
[20] M. Parhizi, A. Jain, G. Kilaz, J.K. Ostanek, Accelerating the numerical solution of thermal runaway in Li-ion batteries, J. Power Sources 538 (2022) 231531, https://doi.org/10.1016/j.jpowsour.2022.231531.
[21] D. Mishra, A. Jain, Multi-mode heat transfer simulations of the onset and propagation of thermal runaway in a pack of cylindrical Li-ion cells, J. Electrochem. Soc. 168 (2021), https://doi.org/10.1149/1945-7111/abdc7b (020504: 1-11).
[22] S. Wang, L. Lu, D. Ren, X. Feng, S. Gao, M. Ouyang, Experimental investigation on the feasibility of heat pipe-based thermal management system to prevent thermal runaway propagation, J. Electrochem. Energy Convers. Storage 16 (2019) 031006, https://doi.org/10.1115/1.4042555.
[23] M.S. Patil, J.H. Seo, M.Y. Lee, A novel dielectric fluid immersion cooling technology for Li-ion battery thermal management, Energy Convers. Manag. 229 (2021) 113715, https://doi.org/10.1016/j.enconman.2020.113715.
[24] J. Xu, C. Lan, Y. Qiao, Y. Ma, Prevent thermal runaway of lithium-ion batteries with minichannel cooling, Appl. Thermal Eng. 110 (2017) 883–890, https://doi.org/10.1016/j.applthermaleng.2016.08.151.
[25] W. Luo, L. Zhao, M. Chen, The effect of PCM on mitigating thermal runaway propagation in lithium-ion battery modules, Appl. Therm. Eng. 236 (2024) 121608, https://doi.org/10.1016/j.applthermaleng.2023.121608.
[26] Y. Huang, J. Lu, Y. Lu, B. Liu, Investigation into the effects of emergency spray on thermal runaway propagation within lithium-ion batteries, J. Energy Storage 66 (2023) 107505, https://doi.org/10.1016/j.est.2023.107505.
[27] J. Fang, J. Cai, X. He, Experimental study on the vertical thermal runaway propagation in cylindrical lithium-ion batteries: effects of spacing and state of charge, Appl. Therm. Eng. 197 (2021) 117399, https://doi.org/10.1016/j.applthermaleng.2021.117399.
[28] S.J. Drake, D.A. Wetz, J.K. Ostanek, S.P. Miller, J.M. Heinzel, A. Jain, Measurement of anisotropic thermophysical properties of cylindrical Li-ion cells, J. Power Sources 252 (2014) 298–304, https://doi.org/10.1016/j.jpowsour.2013.11.107.
[29] D.P. Dewitt, T.L. Bergman, A.S. Lavine, F.P. Incropera, Fundamentals of Heat and Mass Transfer, 6th ed., John Wiley & Sons, 2006 (ISBN: 978-0471457282).
[30] G.-H. Kim, A. Pesaran, R. Spotnitz, A three-dimensional thermal abuse model for lithium-ion cells, J. Power Sources 170 (2007) 476–489, https://doi.org/10.1016/j.jpowsour.2007.04.018.
[31] T. Hatchard, D. MacNeil, A. Basu, J. Dahn, Thermal model of cylindrical and prismatic lithium-ion cells, J. Electrochem. Soc. 148 (2001) A755, https://doi.org/10.1149/1.1377592.
[32] M. Parhizi, J. Ostanek, J.A. Jeevarajan, Three-dimensional thermal resistance network model for thermal runaway in lithium-ion batteries, in: 49th Power Sources Conference, Fort Washington, MD, 2023.
[33] A. Gudi, S. Bonala, CFD Modeling of 18650 Lithium-Ion Cell to Predict Cell Gas Venting and Gas Phase Reactions during Thermal Runaway Event (No. 2024-28-0091), SAE Technical Paper, 2024, https://doi.org/10.4271/2024-28-0091.